

Article

# Effect of Acidic Strength of Surface Ligands on the Carrier Relaxation Dynamics of Hybrid Perovskite Nanocrystals

Sudhakar Narra <sup>1,2</sup> , Po-Sen Liao <sup>1</sup>, Sumit S. Bhosale <sup>1</sup> and Eric Wei-Guang Diao <sup>1,2,\*</sup>

<sup>1</sup> Department of Applied Chemistry, National Yang Ming Chiao Tung University, Hsinchu 300093, Taiwan; sudhakar@nycu.edu.tw (S.N.); sam062986@gmail.com (P.-S.L.); sumitbhosale50@gmail.com (S.S.B.)

<sup>2</sup> Center of Emergent Functional Matter Science, National Yang Ming Chiao Tung University, Hsinchu 300093, Taiwan

\* Correspondence: diau@nycu.edu.tw

**Abstract:** Perovskite nanocrystals (PeNCs) are known for their use in numerous optoelectronic applications. Surface ligands are critical for passivating surface defects to enhance the charge transport and photoluminescence quantum yields of the PeNCs. Herein, we investigated the dual functional abilities of bulky cyclic organic ammonium cations as surface-passivating agents and charge scavengers to overcome the lability and insulating nature of conventional long-chain type oleyl amine and oleic acid ligands. Here, red-emitting hybrid PeNCs of the composition  $Cs_xFA_{(1-x)}PbBr_yI_{(3-y)}$  are chosen as the standard (Std) sample, where cyclohexylammonium (CHA), phenylethylammonium (PEA) and (trifluoromethyl)benzylammonium (TFB) cations were chosen as the bifunctional surface-passivating ligands. Photoluminescence decay dynamics showed that the chosen cyclic ligands could successfully eliminate the shallow defect-mediated decay process. Further, femtosecond transient absorption spectral (TAS) studies uncovered the rapidly decaying non-radiative pathways; i.e., charge extraction (trapping) by the surface ligands. The charge extraction rates of the bulky cyclic organic ammonium cations were shown to depend on their acid dissociation constant (pKa) values and actinic excitation energies. Excitation wavelength-dependent TAS studies indicate that the exciton trapping rate is slower than the carrier trapping rate of these surface ligands.

**Keywords:** perovskite nanocrystals; red emission; surface ligands; defect passivation; charge extraction; exciton; femtosecond TAS



**Citation:** Narra, S.; Liao, P.-S.; Bhosale, S.S.; Diao, E.W.-G. Effect of Acidic Strength of Surface Ligands on the Carrier Relaxation Dynamics of Hybrid Perovskite Nanocrystals. *Nanomaterials* **2023**, *13*, 1718. <https://doi.org/10.3390/nano13111718>

Academic Editor: Jin Soo Kim

Received: 29 April 2023

Revised: 15 May 2023

Accepted: 19 May 2023

Published: 24 May 2023



**Copyright:** © 2023 by the authors. Licensee MDPI, Basel, Switzerland. This article is an open access article distributed under the terms and conditions of the Creative Commons Attribution (CC BY) license (<https://creativecommons.org/licenses/by/4.0/>).

## 1. Introduction

Organic-inorganic halide perovskite nanocrystals (PeNCs) in the form  $ABX_3$  (A = organic/inorganic cations like Cesium cation ( $Cs^+$ ), methylammonium cations (MA), and formamidinium cations (FA); B =  $Pb^{2+}$  or  $Sn^{2+}$ ; X =  $Cl^-$ ,  $Br^-$  or  $I^-$ ) are now popularly being used in many applications such as LEDs, solar cells, photodetectors, photocatalysts, and so on [1–8]. The advantage of choosing these PeNCs over conventional semiconductors is their ease of preparation, impressive device performances, and the tunability of their excellent optoelectronic properties [3,9]. The competitive device performances of PeNCs are attributed to the low defect density and high activation energies required for the formation of deep defects. The major hurdles for commercializing PeNCs are their long-term stability, ion migration, hysteresis, and degradation caused by oxygen and water vapor [10–14].

The surface chemistry of the encapsulating ligands plays a prominent role in modulating the optical properties and stabilities of the PeNCs [3,8,13,15–24]. Conventionally, PeNCs synthesized by the hot injection/addition methods utilize oleylamine (OLA) and oleic acid (OA) as encapsulating ligands [1,25]. The labile nature of these ligands leads to the loss of surface ligands during purification [25], affecting the stability, whereas the insulation nature of these ligands inhibits efficient charge conduction [23]. Several surface engineering strategies have been worked out to passivate the surface defects and improve the charge conduction properties of the PeNCs [15,18,19,24,26–32]. Among them,

utilizing cyclic aromatic cations to simultaneously passivate the surfaces and induce interfacial energy transfer is an interesting approach to boost the conduction properties of the PeNCs [15,26,27]. The acid–base chemistry between the uncoordinated lead ions and the encapsulating surface ligands is of importance, as the former, being a soft acid, prefers a soft base to achieve efficient passivation of the surface [17,31]. Despite efficient passivation by soft base-type ligands, the photoluminescence quantum yields in most of the cases are less than unity [19]. The mechanisms of the non-radiative losses induced by passivating ligands need deeper understanding.

In this study, we show the passivating effects of the bulky cyclic/aromatic cations (short-chain ligands) on synthesized red-emitting  $\text{Cs}_x\text{FA}_{(1-x)}\text{PbBr}_y\text{I}_{(3-y)}$  (CsFA) PeNCs. The short-chain ligands used to passivate the surfaces of CsFA PeNCs are cyclohexylammonium (CHA), phenylethylammonium (PEA) and 4-(trifluoromethyl)benzylammonium (TFB). Photoluminescence decay studies show efficient passivation of shallow trap states by these short-chain ligands. Further, femtosecond transient absorption spectral (TAS) experiments have been performed to uncover the nonradiative losses in the PeNCs. It is shown that surface ligands are responsible for the ultrafast nonradiative losses induced in these PeNCs, and the rates of trapping are shown to correlate with the pKa values of the surface ligands.

## 2. Materials and Methods

### 2.1. Chemicals

Lead iodide ( $\text{PbI}_2$ ) (purity 99%, Sigma Aldrich, St Louis, MO, USA), Cesium carbonate ( $\text{Cs}_2\text{CO}_3$ ) (purity 99%, Thermo Fisher Scientific, Germany), Formamidinium bromide (FABr) (purity 99%, Greatcell Solar Materials, Queanbeyan, NSW, Australia), Phenylethylammonium iodide (PEAI) (purity 99%, Greatcell Solar Materials, Queanbeyan, NSW, Australia), Cyclohexylmethylammonium iodide (CHAI) (purity 99%, Greatcell Solar Materials, Queanbeyan, NSW, Australia), 4-Trifluoromethyl-benzylammonium iodide (TFBI) (purity 99%, Greatcell Solar Materials, Queanbeyan, NSW, Australia), Oleylamine (OLA) (Technical grade, purity 70%, Sigma Aldrich, Zwijndrecht, The Netherlands), Oleic acid (OA) (Technical grade, purity 90%, Sigma Aldrich, Zwijndrecht, The Netherlands), Octadecene (Technical grade, purity 90%, Sigma Aldrich, St. Louis, MO, USA), Hydriodic acid (57% in water, Alfa Aesar, Kandel, Germany), Isopropanol (IPA) (anhydrous, purity 99.5%, Sigma Aldrich, Steinheim am Albuch, Germany), Methyl acetate (Purity 99%, Thermo Fisher Scientific, Germany), Octane (Purity 99.8%, J T Baker Chemicals B V., Deventer, The Netherlands).

### 2.2. Synthesis of Perovskite Nanocrystals

The PeNCs used in this work were synthesized using the one-pot sequential hot addition method (HAM) reported elsewhere [33]. CsFA PeNCs were prepared from the precursor solutions of  $\text{Cs}_2\text{CO}_3$ , FABr, and  $\text{PbI}_2$ , whereas surface passivation of CsFA PeNCs were performed by adding the precursor solutions of the bulky organic cations. A volume of 0.94 mmol of  $\text{Cs}_2\text{CO}_3$  precursor solution was prepared by adding 3 mL of OA and 3 mL of octadecane to a 20 mL vial, and the resultant mixture was heated at 150 °C until the solution became transparent. A volume of 1.88 mmol FABr solution was prepared by dissolving precursor salt in 3 mL IPA. Then, 1.88 mmol of  $\text{PbI}_2$  in octadecane was taken in a 50 mL round-bottomed (RB) flask and stirred for one hour at 100 °C to remove water. Later, 5 mL each of OA and OLA were added to dissolve the  $\text{PbI}_2$ . The  $\text{PbI}_2$  solution changes from turbid to clear after complete dissolution of  $\text{PbI}_2$ . The temperature of the  $\text{PbI}_2$  solution was further raised to 140 °C and the FABr solution was added. The reaction mixture turned a turbid orange color in the RB flask. The temperature was slowly increased, and the solution turned to light yellow color from turbid orange color during this process. When the temperature became 200 °C, 6 mL of cesium oleate was added to the reaction mixture, and then the RB flask carrying the reaction mixture was immediately immersed in an ice bath to arrest the further growth of the PeNCs to the black phase. This completed the synthesis of FACs PeNCs. The surface-passivated PeNCs' synthesis involves an additional

step, wherein 1.88 mmol of the corresponding bulky organic ammonium iodides (CHAI, PEAI, and TFBI) in IPA were added to the reaction mixture together with the FABr before the injection of cesium oleate. The synthesized PeNCs were purified using repetitive washing and centrifugation methods as described. Crude PeNC solution was centrifuged at 9000 rpm for 40 min. The precipitate containing large particles was discarded. The supernatant is the desired PeNC sample of the desired size. The surface-passivated PeNCs need further purification. Methyl acetate is added at a ratio of 1:3 to precipitate PeNCs. The precipitates collected by centrifugation were finally dispersed in octane to obtain the final products. The synthesized PeNCs are reported to display a relative photoluminescence quantum yield of 0.72, 0.76, 0.70, and 0.69, respectively for Std, CHA, PEA, and TFB samples [33]. The pKa values of the short-chain ligands were obtained by measuring the pH of the corresponding 0.1 M aqueous salt solutions.

### 2.3. Optical Characterizations

UV-Visible absorption spectra of PeNCs samples were measured using a JASCO V-780 absorption spectrophotometer equipped with a JASCO integration sphere accessory. The absorption spectra of PeNC samples were measured with a custom cell holder equipped with BK9 glass windows with an optical pathlength of 0.2 mm. The absorption spectra of the samples were corrected for reflection and scattering effects. The absorbance of the PeNC samples was estimated using Equation (1) as shown below.

$$A = -\log\left(\frac{I_T}{(I_0 - I_R)}\right) \quad (1)$$

where  $I_0$  and  $I_T$  are the transmittances of the reference light and samples, respectively, and  $I_R$  is the reflectance of the sample.

The PL spectra of the PeNC samples were measured using a customized PL spectrometer. The PL spectrometer is equipped with a 150 W Xe lamp from OBB as a light source. The excitation wavelength was chosen using a Horiba microHR spectrometer (1200 groves grating, blaze wavelength: 330 nm). The emission from the sample was collected using a TRIAX spectrometer (600 groves grating, blaze wavelength: 500 nm). The collected emission was focused on the exist slit of the monochromator, collected by the photomultiplier tube connected to the preamplifier. The signal was digitized using a SpecACQ2 digitizer. All the electronic components are controlled by software in a coordinated way to obtain the PL spectrum. The excitation wavelength was set to 450 nm for measuring the PL spectrum of the samples. The excitation light scattering was minimized by using a 480 nm long pass color glass filter on the emission side of the spectrometer.

The PL lifetime measurements of PeNC samples were performed using a PicoQuant FluoTime 200 fluorescence lifetime spectrometer. The PeNCs were excited using a 375 nm picosecond diode laser pulse (LDH-P-C -375, FWHM: 60 ps), controlled by a diode laser driver PLD 200-B. The emission from the sample was collected by a double monochromator and detected using a high-speed microchannel plate photomultiplier tube (MCP-PMT). The MCP-PMT output was controlled and digitized by a PicoHarp 300 controller. The PL lifetimes of PeNCs were measured in the range of 620–640 nm.

The fs-transient absorption spectra were acquired using an Excipro ultrafast pump-probe absorption spectrometer (CDP systems). The TAS spectrometer was coupled with a femtosecond Ti: Sapphire amplified laser system (Coherent Legend USP, 795 nm, 1 kHz, 3 mJ, 35 fs), optical parametric amplifiers (TOPAS-C), and a sapphire plate for generating femtosecond pump and probe pulses. The details of the TAS system are described elsewhere [34]. Briefly, 480 nm and 640 nm pump pulses generated from TOPAS-C are used for the above bandgap and the near-resonant pumping of PeNC samples dispersed in an octane solution. The probe pulses are generated by focusing the weaker portion of the fundamental beam on a sapphire plate to generate a white light continuum, which is limited to 750 nm using a short pass filter. The pump-induced changes in the absorption of the sample are measured by optically modulating the pump pulses using an optical

chopper. The fluctuation in the probe light spectrum is nullified by referencing the probe light. The time-dependent absorption changes in the sample are obtained by delaying the pump pulses with respect to the probe pulse. The polarization between pump and probe pulses is set to a magic angle to suppress the coherent artifacts. The transient absorption spectra are corrected for the white light dispersion using the optical Kerr signals of the solvent [35], and denoised using singular value decomposition (SVD) analysis.

### 3. Results

The schematic of CsFA PeNCs (Std) with surface-passivating long-chain ligand OLA and halogen vacancies is shown in Figure 1a. The halogen vacancies on the surface were passivated using the short-chain ligands CHA, PEA, and TFB as shown in Figure 1a,c, respectively. Further, the surface-passivating effects of short-chain ligands CHA, PEA, TFB on the Std PeNCs were examined using the optical spectroscopic techniques described below. The surface-passivated PeNCs hereafter are referred to using their ligand abbreviation names.

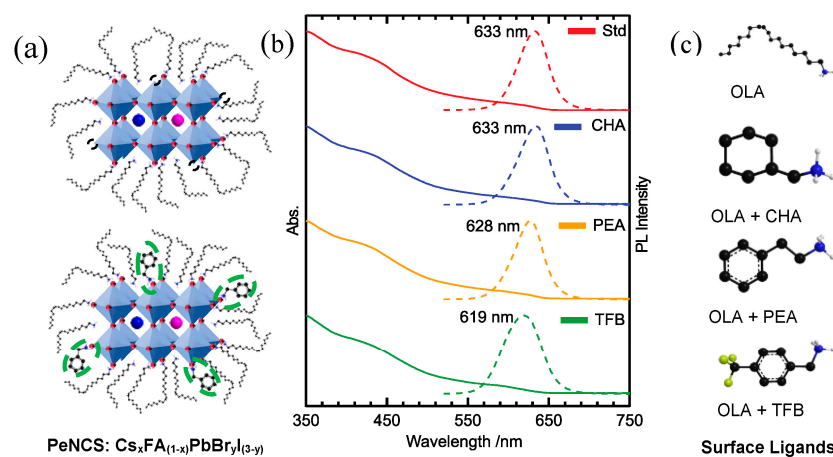


**Figure 1.** (a) Schematic of  $\text{Cs}_x\text{FA}_{(1-x)}\text{PbBr}_y\text{I}_{(3-y)}$  PeNCs showing halogen vacancies and their passivation by short-chain ligands, (b) UV-PL spectra of Std, CHA, PEA and TFB PeNC samples and (c) chemical structures of surface-passivating short-chain ligands.

#### 3.1. UV-PL Spectroscopy

UV-Vis absorption and PL spectra of PeNCs are shown in Figure 1b. The absorption spectra of nanocrystal samples show the onset of absorption at 620 nm, while their emission peaks were centered at  $626 \pm 7$  nm, indicating that the synthesized nanocrystals are red-emitting nanocrystals suitable for red LED applications with a narrow bandwidth of 20 nm. The modest shifts in PL peak positions between the samples might be due to the modulation of the composition proportions. It is worth mentioning that all optical measurements are performed from diluted samples/thinner path length cell holders to maintain similar optical densities for comparison purposes, and also to minimize the reabsorption effects on the PL spectra. These precautions were taken to carefully evaluate the passivating ligands' effects on the optical properties of the samples.

Further, the UV-Vis absorption spectra of the PeNC samples were fitted using Elliot's equations (Figure S1) described elsewhere [36–38]. The bandgaps estimated from Elliot's fit (Table S1) correlate well with the corresponding sample's PL emission maximum, whereas the estimated exciton-binding energies (Table S1) are extremely small, implying excitons can split to free carriers easily, which is a common phenomenon for large-sized crystals [38,39].

#### 3.2. TCSPC Decay Kinetics

The TCSPC decay profiles of PeNC samples are shown in Figure 2. The decay profiles shown in Figure 2 were collected from respective PL maxima. The TCSPC decay profiles of PeNCs show an instantaneous rise and a complete decay within 400 ns. The transient decay

profiles were fitted using either exponential or stretched exponential functions. The Std PeNCs samples fit well to the bi-exponential decaying function described by Equation (2), while the CHA, PEA, and TFB samples were fitted to a stretched exponential function described by Equation (3).

$$I(t) = A_1 \exp\left(-\frac{t}{\tau_1}\right) + A_2 \exp\left(-\frac{t}{\tau_2}\right) \quad (2)$$

$$I(t) = A \exp\left(-\frac{t}{\tau}\right)^\beta \quad (3)$$

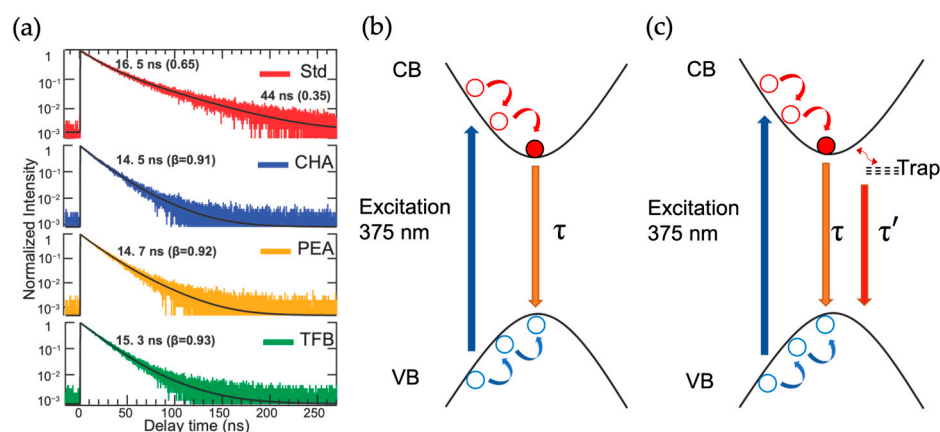


**Figure 2.** (a) Overlay of TCSPC decay profiles and curve fits of Std, CHA, PEA, and TFB PeNCs. The decay profiles were monitored at their respective PL maxima positions of the samples. (b,c) PL decay mechanism for the surface-passivated and standard PeNC samples, respectively.

Here,  $A_1$ ,  $A_2$ , and  $A$  are preexponential factors,  $\tau_1$ ,  $\tau_2$ , and  $\tau$  are time coefficients, and  $\beta$  (which lies between 0 and 1) is the stretching exponent that expresses the degree of asymmetry of the synthesized PeNCs.

The Std PeNC decays with time constants of 16.5 ns and 44 ns, as shown in Figure 2, whereas surface-passivated samples decay with a time constant of 15 ns and  $\beta$  close to unity (mono-exponential behavior), indicating that the samples are either homogenous in nature or the emission centers of the PeNCs are of similar origin. Wavelength-dependent decay profiles (Figure S2) display longer lifetimes on the longer wavelength side of their respective emission spectra, which is indicative of inter-crystal energy transfer in the PeNCs due to exciton hopping [39,40]. Further, the observed 16.5 ns and 44 ns decaying time constants for the Std PeNC sample were attributed to direct and shallow trap state-mediated recombination, as described by Figure 2c. The assignments of the faster decaying components to direct recombination and slower recombination with delayed luminescence caused by shallow trap states has also been observed for other types of PeNC samples [41,42]. The effective surface-passivating nature of the bulky organic ligands is clearly described by their TCSPC decay profiles, as the shallow trap state-mediated recombination is completely quenched, as shown in the relaxation mechanism in Figure 2b. However, the TCSPC results presented in this section are limited to the sub-nanosecond and nanosecond decay dynamics, the nonradiative processes occurring in the sub-picosecond time scales, and the reasons for the non-unity PLQY are scant in these studies. Hence, fs TAS experiments were performed to uncover the faster dynamics of the PeNC samples.

### 3.3. TAS Decay Dynamics: Above Bandgap Excitation

The TAS profiles of PeNC samples for the above bandgap excitation condition were performed by exciting the samples using 480 nm actinic pump pulses, and probing between 530 and 730 nm using broadband white-light continuum pulses, as shown in Figure 3.

The top panels show the evolution of the TAS profiles acquired between 0–2 ps of pump–probe delay times, whereas the bottom panels display the subsequent recombination of the TAS profiles acquired between 5–800 ps of pump–probe delay times. The TAS profile shapes of all PeNC samples resemble each other, except for the differences in their bleach minima positions and their decay dynamics. Further, the TAS profiles shown between 0–2 ps reflect the signatures of hot carrier distributions, as described earlier [43,44], whereas recombination decays at later stages can be seen in the TAS profiles shown between 5–800 ps. The decay-assisted decomposition of TAS profiles was deconvoluted using the modeling of the kinetic profiles using a relaxation scheme which will be discussed later.

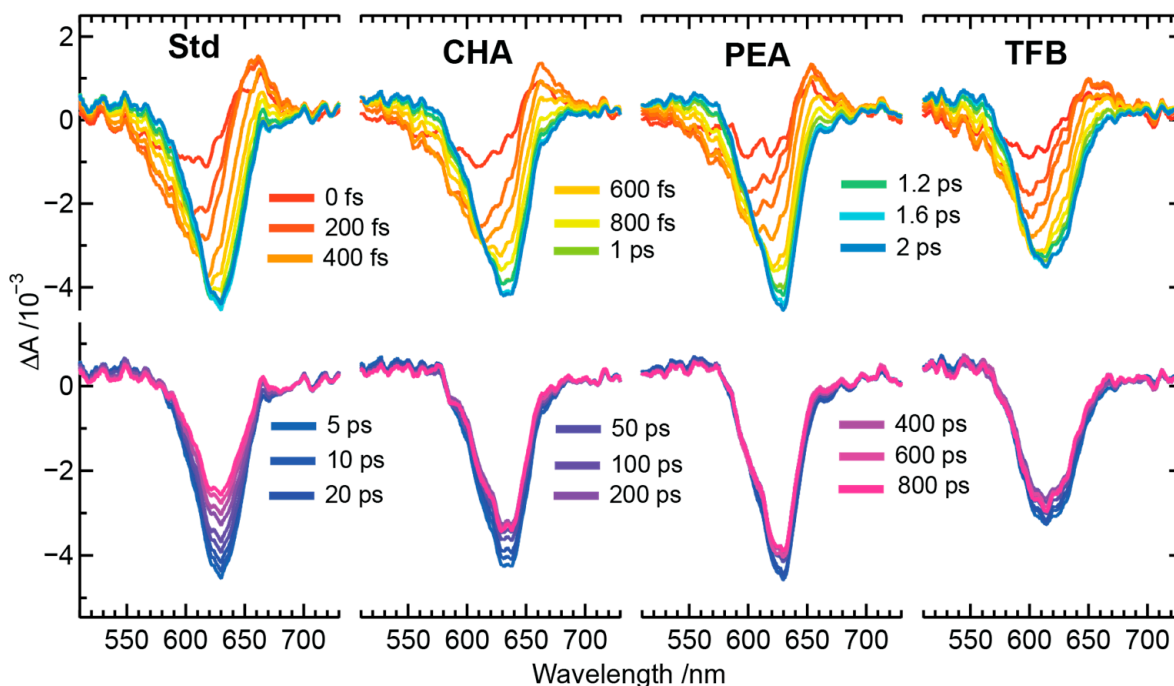


**Figure 3.** TAS profiles of Std, CHA, PEA, and TFB PeNC samples of the composition  $\text{Cs}_x\text{FA}_{(1-x)}\text{PbBr}_y\text{I}_{(3-y)}$ . The actinic excitation wavelength for the samples was set to 480 nm.

### 3.4. TAS Decay Dynamics: Near-Resonant Excitation

The TAS profiles of PeNC samples in the near-resonant excitation condition was performed by exciting the samples using 640 nm actinic excitation pulses, while the probing region is set similar to the above band gap excitation, as shown in Figure 4. Near-resonant excitation experiments were performed to eliminate the hot carrier profiles from the TAS profiles and focus only on the recombination dynamics of the excitons or cold carriers. Similar to the above band gap excitation, the top panels show the evolution of the TAS profiles acquired between 0–2 ps of pump–probe delay times, whereas the bottom panels display the subsequent recombination of the TAS profiles acquired between 5–800 ps of pump–probe delay times. The TAS profile shapes of all PeNC samples acquired under near-resonant conditions are sharper and smoother than the above bandgap excitations. The sharper band shapes confirm the absence of hot carriers under near-resonant conditions, whereas smoother band shapes could be due to weaker scattering from the PeNCs under 640 nm excitation. Further, the TAS profiles shown between 0–2 ps display no photoinduced absorption (PIA) band on the blue side of the PB band, unlike the above bandgap excitation. The PIA band on the blue side of the PB band is assigned to the population of forbidden excitonic state due to the breaking of inversion symmetry for PeNCs [45]. The decay-assisted decomposition of TAS profiles was deconvoluted using the modeling of the kinetic profiles, using a relaxation scheme which will be discussed later.

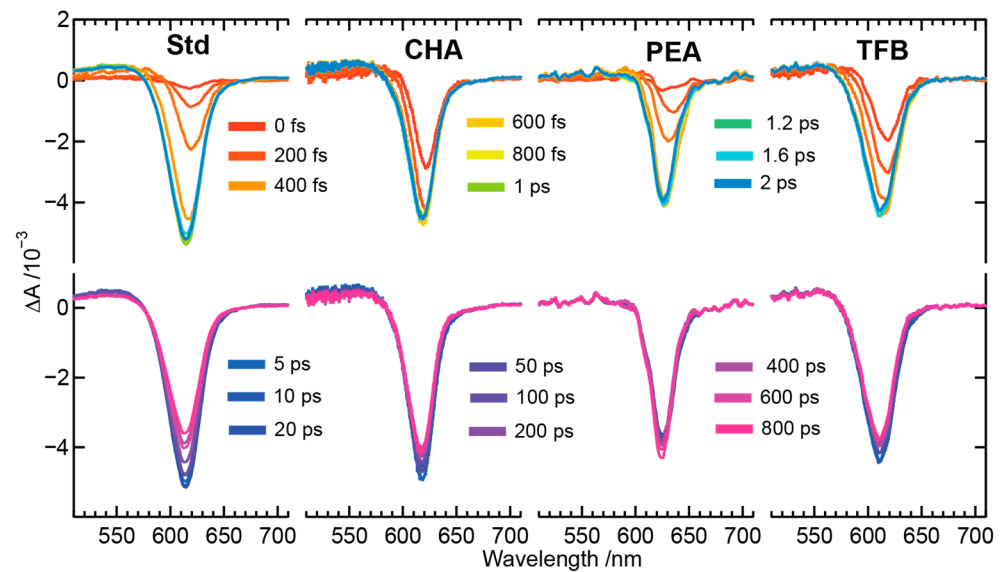


**Figure 4.** TAS profiles of perovskite nanocrystals of the composition  $\text{Cs}_x\text{FA}_{(1-x)}\text{PbBr}_y\text{I}_{(3-y)}$  (Std), and surface-passivated perovskite crystals with bulkier organic ligands referred as CHA, PEA, and TFB in the display panel. The excitation wavelength of the perovskite nanocrystals was set to 640 nm.

### 3.5. Decay-Assisted Spectral Deconvolution: Kinetic Modeling of TAS Profiles

The TAS profile spectrograms were subjected to singular-value decomposition (SVD) analysis for both the above bandgap and near-resonant excitation conditions to find the minimum resolvable spectral features in both of the experiments. SVD analysis suggests that at least three components (Figure S3) are required to model the relaxation kinetics based on their decay dynamics. Based on spectral features and energies of excitation, a free carrier model is applied for above band gap excitation, whereas the exciton model is applied for near-resonant excitation, as shown in Figure 5. The choice of the models can be justified as the above bandgap excitation energy is sufficient to split the weakly binding excitons to hot carriers, and similarly, resonant excitation with the excitonic transitions should deplete exciton bands, yielding more excitons, as evidenced by the sharp PB bands for the near-resonant excitation condition.

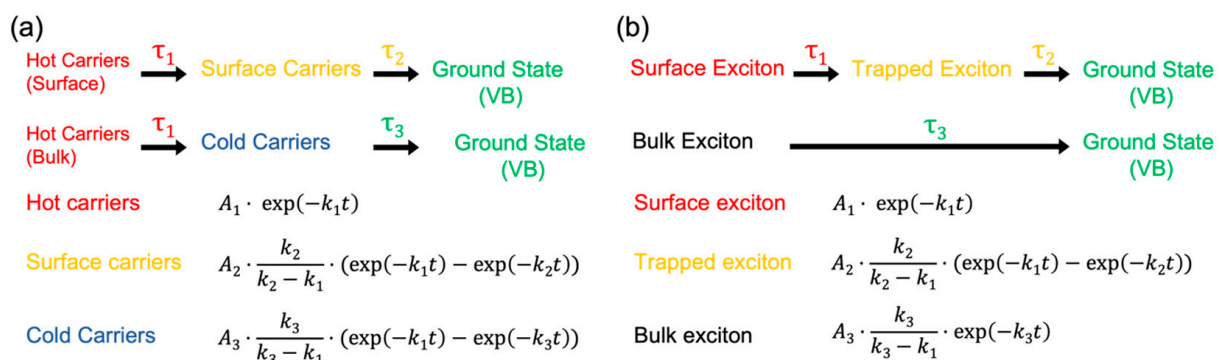


**Figure 5.** Carrier (a) and exciton (b) relaxation kinetic models for PeNCs under 480 nm (above band gap) and 640 nm (near-resonance) excitation conditions, respectively.

The kinetic models described in Figure 5 are sequential parallel models describing the heterogeneous carrier/exciton relaxation processes, namely in the bulk and in the proximity of surface defects. Photoexcitation with actinic excitation pulses produces an excess hot carriers/excitons depending on the excitation energy, which progressively cools down and leads to recombination of cold carriers in bulk PeNC, whereas the hot carriers/excitons when produced close to the proximity of surface defect will be captured by the defect sites,

which are referred to as surface carriers/excitons. They recombine non-radiatively via an alternative pathway to that of bulk PeNC. The wavelength-dependent TAS profiles shown in Figures S4–S11 were fitted to their respective kinetic models to deconvolute the decay-assisted spectra, as shown in Figure 6. The kinetic models are validated by global fitting of the TAS kinetic profiles at all probe wavelengths. Further residual maps shown in Figures S4–S11 were checked to see the authenticity of the data fitting according to the kinetic model (Figure 5). The featureless residual maps confirm the validity of our fitting approach. The fitting coefficients obtained from the curve fitting of TAS profiles using the kinetic models are shown in Tables 1 and 2.

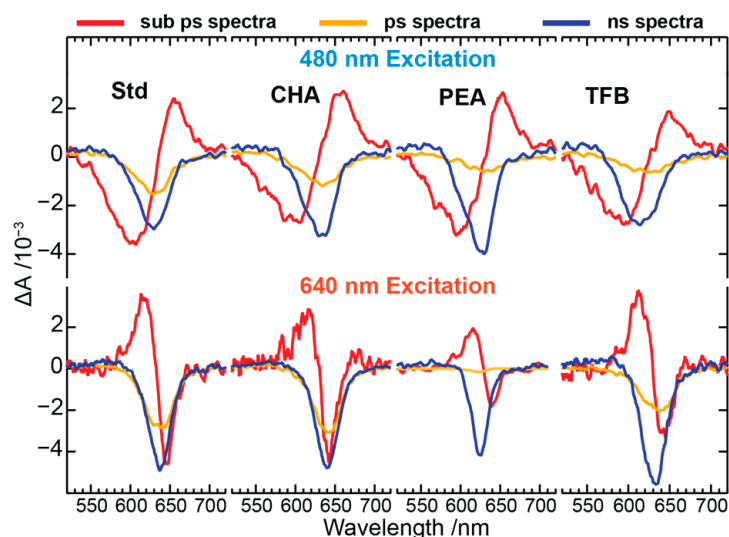


**Figure 6.** Decay-assisted deconvoluted spectral profiles of Std, CHA, PEA, and TFB PeNCs of the composition  $Cs_xFA_{(1-x)}PbBr_yI_{(3-y)}$  (Std).

**Table 1.** Carrier model fitting coefficients obtained from the global fitting of TAS profiles obtained using 480 nm actinic excitation pulses.  $\tau_1$  is the hot carrier cooling time,  $\tau_2$  is surface carrier recombination time and  $\tau_3$  is the ns offset.

Sample	$\tau_1$ (ps)	$\tau_2$ (ps)
Std.	0.5	108
CHA	0.6	42
PEA	0.5	45
TFB	0.5	22

**Table 2.** Exciton model fitting coefficients obtained from the global fitting of TAS profiles obtained using 640 nm actinic excitation pulses.  $\tau_1$  is the hot carrier cooling time,  $\tau_2$  is surface exciton recombination time and  $\tau_3$  is the ns offset.

Sample	$\tau_1$ (ps)	$\tau_2$ (ps)
Std.	0.1	168
CHA	0.1	92
PEA	0.2	100
TFB	0.1	49

The hot carrier/exciton cooling times are shown to be independent of the surface ligand passivation effects, as shown in Tables 1 and 2, with a cooling time of 0.5 and 0.1 ps, respectively, for the hot carriers and excitons. However, surface carrier/exciton recombination time coefficients showed similar changes with changes in the composition of the surface ligands, as shown in Tables 1 and 2. The surface carriers/exciton recombination



seem to correlate with the  $pK_a$  values of the surface ligands. The estimated  $pK_a$  values of the surface ligands decrease in the order of PEA (12.14) > CHA (11.68) > TFB (10.89). The surface carrier/exciton recombination also follows the same order as the  $pK_a$ , with pristine samples being slowest due to the insulating nature of the OA/OA ligands. The smaller the  $pK_a$  the higher the affinity to accept the electrons.

#### 4. Discussion

The PL lifetimes of PeNCs showed both radiative and delayed luminescence processes on the nanosecond timescale, whereas TAS results demonstrate a non-radiative channel with a timescale of under 100 ps. The delayed luminescence process occurring in the nanosecond timescales are often attributed to shallow defects stemming from iodine vacancies, whereas the picosecond non-radiative processes shown in this work could be due to the charge or exciton transfer/trapping to the surface-passivating ligand, as shown elsewhere [41,46]. The short-chain surface ligands successfully blocked the shallow trap-mediated recombination; however, they opened up another charge/exciton funneling channel. So, DFT calculations (basis: B3LYP/631 + g(d, p), charge: singlet) were performed to estimate the HOMO and LUMO levels of the surface ligands to check the energetic alignments with that of pristine  $\text{CsPbBr}_3$  and  $\text{CsPbI}_3$  nanocrystals, as shown in Figure 7c. The LUMO levels of the ligands lie deeper in the forbidden gap of PeNCs, and therefore the picosecond non-radiative recombination process observed in the TAS experiments could be that of charge/exciton trapping to the surface ligand, whose rates correlate well with the  $pK_a$  values of the ligands. Further, the relaxation model showing the charge and exciton trapping under the above band gap and resonant excitations are shown in Figures 7a and 7b, respectively. The above bandgap produces hot carriers that cool within about  $\sim 0.5$  ps ( $\tau_1$ ), and surface ligand-mediated recombination occurs within 100 ps ( $\tau_2$ ), following Std (108 ps) > PEA (45 ps) > CHA (42 ps) > TFB (22 ps), whereas band-to-band ( $\tau_3$ ) and shallow trap-mediated recombination ( $\tau'$ , only for Std sample) occur on nanosecond timescales, as described in the TCSPC decay section. Similarly, resonant excitation produces hot excitons that are rapidly trapped by surface ligands within 0.1 ps ( $\tau_1$ ), and the surface ligand-trapped excitons ( $\tau_2$ ) recombine slightly slower than the trapped carriers as follows: Std (168 ps) > PEA (100 ps) > CHA (92 ps) > TFB (49 ps). However, band-to-band ( $\tau_3$ ) and shallow trap-mediated recombination ( $\tau'$ , only for Std sample) occur in nanosecond timescales. Further, it is interesting to note that  $pK_a$  is the dominating effect, rather than the aromaticity, as CHA and PEA samples display similar charge-trapping rates due to their closer  $pK_a$  values.

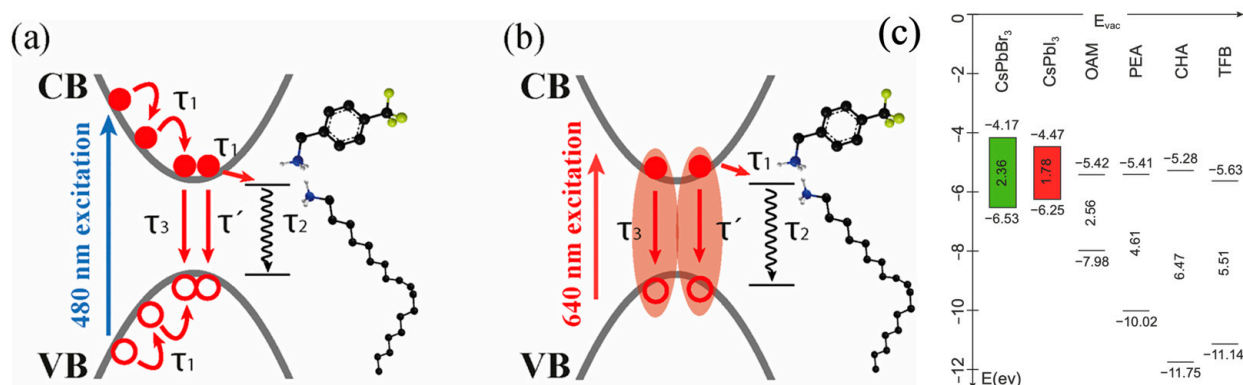


**Figure 7.** Relaxation mechanism of  $\text{Cs}_x\text{FA}_{(1-x)}\text{PbBr}_y\text{I}_{(3-y)}$  perovskite nanocrystals under (a) 480 nm and (b) 640 nm excitation conditions. (c) HOMO-LUMO estimations of the bulkier cyclic aromatic cations using DFT method. The VB and CB band positions of  $\text{CsPbBr}_3$  and  $\text{CsPbI}_3$  were taken from the literature [47].

The PL decay and TAS results presented in this study show both the passivation and charge-scavenging nature of the surface ligands. The charge separation/scavenging caused by the short-chain ligands may be beneficial for photovoltaic or photocatalytic applications in which charges have to be extracted, whereas in the scenarios of retaining the radiative recombination, surface ligands with weaker acidity are preferred. A surface ligand with weak acidity is also less prone to deprotonation, which is beneficial for the long-term stability of the PeNCs.

## 5. Conclusions

Red-emitting PeNCs of the composition  $Cs_xFA_{(1-x)}PbBr_yI_{(3-y)}$  were shown to have emission at  $626 \pm 7$  nm, with small exciton binding energies. The short-chain ligands CHA, PEA, and TFB cations used in this study are shown to exert weak modulation on the electronic bandgap. The TCSPC decay profiles of the Std PeNCs were shown to decay with two decaying time coefficients of 16.5 ns (direction recombination) and 44 ns (shallow-trap mediated recombination), respectively, while short-capping ligand-passivated samples decay via a stretched exponential function with uniform time coefficients of about 15 ns, and the stretch factor  $\beta$  is close to 0.9. The absence of long-lived decay components in the CHA, PEA, and TFB samples confirms the passivation effects of the short-chain ligands. Femtosecond TAS studies of the nanocrystals using 480 nm excitation show the spectral signatures of hot carriers, surface carriers, and cold carriers. The hot carriers recombine with 0.5 ps for all samples, and cold carrier recombination was not complete, while the surface carrier recombination rates show variation in the order Std (108 ps) > PEA (46 ps) > CHA (42 ps) > TFB (22 ps). The increased reaction rates of surface carriers can be explained based on the pKa, as the pKa shows the order PEA (12.14) > CHA (11.68) > TFB (10.89). The decrease in pKa is associated with the increased electron-accepting ability of the ligands. The charge losses at the surface of ligands were ascribed to the non-unity PLQY of these red-emitting nanocrystals. Femtosecond TAS studies of the PeNCs under resonant excitation showed the spectral signatures of the bulk exciton, surface exciton, and trapped exciton. It is shown that surface exciton becomes trapped in 0.1 ps in all samples, and bulk excitation is not complete in all the samples, while trapped excitons recombine non-radiatively in a similar manner to surface carriers, but with varied decay coefficients: Std (168 ps) > PEA (100 ps) > CHA (92 ps) > TFB (49 ps). The trapped excitons recombine slower when compared to surface carriers due to the variation in the interactions between surface ligands and carriers or excitons.

**Supplementary Materials:** The following supporting information can be downloaded at: <https://www.mdpi.com/article/10.3390/nano13111718/s1>, Figure S1: UV-Vis absorption spectra of (a) Std, (b) CHA, (c) PEA and (d) TFB PeNC samples of the composition  $Cs_xFA_{(1-x)}PbBr_yI_{(3-y)}$  (Std). The band edges of the absorption spectra were fitted to Elliot's model equations, which is expressed as a linear combination of excitonic and continuum states. The contributions of excitonic, continuum and the total fits of the band edges are overlaid on the absorption profiles.; Figure S2: Wavelength dependent TCSPC decay profiles (a) Std, (b) CHA, (c) PEA and (d) TFB PeNC samples of the composition  $Cs_xFA_{(1-x)}PbBr_yI_{(3-y)}$  (Std). The Std sample decay profiles were fitted to a bi-exponential function whereas surface passivated PeNC samples decay profiles were fitted to a stretched exponential function.; Figure S3: Singular value plots (a, e) Std, (b, f) CHA, (c, g) PEA and (d, h) TFB PeNC samples of the composition  $Cs_xFA_{(1-x)}PbBr_yI_{(3-y)}$  (Std). The top and bottom panels results represent 480 and 640 nm excitation conditions. These plots suggests that at least three species are involved in the relaxation dynamics of perovskite nanocrystals irrespective of excitation and surface passivation conditions.; Figure S4: Wavelength dependent transient absorption decay kinetic profiles of (a)  $Cs_xFA_{(1-x)}PbBr_yI_{(3-y)}$  (Std) PeNCs. The decay kinetics were fitted with a kinetic model shown in Figure 5a. The TA data were obtained using 480 nm excitation condition. Spectrogram of Std (b), reconstructed spectrogram (c) obtained from the global curve fitting analysis and residual spectrogram (d) obtained by subtracting b from c. The featureless residual spectrogram serves as a validation of the kinetic model.; Figure S5: Wavelength dependant transient absorption decay kinetic profiles of (a)  $Cs_xFA_{(1-x)}PbBr_yI_{(3-y)}$  PeNCs passivated with short chain ligand CHA. The decay kinetics were

fitted with a kinetic model shown in Figure 5a. The TA data were obtained using 480 nm excitation condition. Spectrogram of CHA (b), reconstructed spectrogram (c) obtained from the global curve fitting analysis and residual spectrogram (d) obtained by subtracting b from c. The featureless residual spectrogram serves as a validation of the kinetic model.; Figure S6: Wavelength dependent transient absorption decay kinetic profiles of (a)  $\text{Cs}_x\text{FA}_{(1-x)}\text{PbBr}_y\text{I}_{(3-y)}$  PeNCs passivated with short chain ligand PEA. The decay kinetics were fitted with a kinetic model shown in Figure 5a. The TA data were obtained using 480 nm excitation condition. Spectrogram of PEA (b), reconstructed spectrogram (c) obtained from the global curve fitting analysis and residual spectrogram (d) obtained by subtracting b from c. The featureless residual spectrogram serves as a validation of the kinetic model.; Figure S7: Wavelength dependent transient absorption decay kinetic profiles of (a)  $\text{Cs}_x\text{FA}_{(1-x)}\text{PbBr}_y\text{I}_{(3-y)}$  PeNCs passivated with short chain ligand TFB. The decay kinetics were fitted with a kinetic model shown in Figure 5a. The TA data were obtained using 480 nm excitation condition. Spectrogram of TFB (b), reconstructed spectrogram (c) obtained from the global curve fitting analysis and residual spectrogram (d) obtained by subtracting b from c. The featureless residual spectrogram serves as a validation of the kinetic model.; Figure S8: Wavelength dependent transient absorption decay kinetic profiles of (a)  $\text{Cs}_x\text{FA}_{(1-x)}\text{PbBr}_y\text{I}_{(3-y)}$  (Std) PeNCs. The decay kinetics were fitted with a kinetic model shown in Figure 5b. The TA data were obtained using 640 nm excitation condition. Spectrogram of Std (b), reconstructed spectrogram (c) obtained from the global curve fitting analysis and residual spectrogram (d) obtained by subtracting b from c. The featureless residual spectrogram serves as a validation of the kinetic model.; Figure S9: Wavelength dependent transient absorption decay kinetic profiles of (a)  $\text{Cs}_x\text{FA}_{(1-x)}\text{PbBr}_y\text{I}_{(3-y)}$  (Std) PeNCs passivated with short chain ligand CHA. The decay kinetics were fitted with a kinetic model shown in Figure 5b. The TA data were obtained using 640 nm excitation condition. Spectrogram of CHA (b), reconstructed spectrogram (c) obtained from the global curve fitting analysis and residual spectrogram (d) obtained by subtracting b from c. The featureless residual spectrogram serves as a validation of the kinetic model.; Figure S10: Wavelength dependent transient absorption decay kinetic profiles of (a)  $\text{Cs}_x\text{FA}_{(1-x)}\text{PbBr}_y\text{I}_{(3-y)}$  (Std) PeNCs passivated with short chain ligand PEA. The decay kinetics were fitted with a kinetic model shown in Figure 5b. The TA data were obtained using 640 nm excitation condition. Spectrogram of PEA (b), reconstructed spectrogram (c) obtained from the global curve fitting analysis and residual spectrogram (d) obtained by subtracting b from c. The featureless residual spectrogram serves as a validation of the kinetic model. Figure S11: Wavelength dependent transient absorption decay kinetic profiles of (a)  $\text{Cs}_x\text{FA}_{(1-x)}\text{PbBr}_y\text{I}_{(3-y)}$  (Std) PeNCs passivated with short chain ligand TFB. The decay kinetics were fitted with a kinetic model shown in Figure 5b. The TA data were obtained using 640 nm excitation condition. Spectrogram of TFB (b), reconstructed spectrogram (c) obtained from the global curve fitting analysis and residual spectrogram (d) obtained by subtracting b from c. The featureless residual spectrogram serves as a validation of the kinetic model. Figure S12: Femtosecond transient absorption spectrograms of (a) Std, (b) CHA, (c) PEA and (d) TFB PeNC samples of the composition  $\text{Cs}_x\text{FA}_{(1-x)}\text{PbBr}_y\text{I}_{(3-y)}$  (Std). The spectrograms were obtained using 480 nm excitation pulses. Figure S13: Femtosecond transient absorption spectrograms of ((a) Std, (b) CHA, (c) PEA and (d) TFB PeNC samples of the composition  $\text{Cs}_x\text{FA}_{(1-x)}\text{PbBr}_y\text{I}_{(3-y)}$  (Std). The spectrograms were obtained using 640 nm excitation pulses; Table S1: Estimations of bandgaps and exciton binding energies obtained from UV-Vis absorption spectral band edge fitting using Elliot model equation for  $\text{Cs}_x\text{FA}_{(1-x)}\text{PbBr}_y\text{I}_{(3-y)}$  (Std) and surface passivated perovskite nanocrystals with bulky organic ligands CHA, PEA, and TFB.

**Author Contributions:** Conceptualization, S.S.B., S.N. and E.W.-G.D.; methodology, S.N. and P.-S.L.; software, S.N.; validation, S.N., P.-S.L. and E.W.-G.D.; formal analysis, P.-S.L. and S.N.; investigation, P.-S.L. and S.N.; samples, S.S.B.; data curation, P.-S.L. and S.N.; writing—original draft preparation, S.N.; writing—review and editing, S.N., P.-S.L., S.S.B. and E.W.-G.D.; visualization, P.-S.L.; supervision, S.N. and E.W.-G.D.; project administration, E.W.-G.D.; funding acquisition, E.W.-G.D. All authors have read and agreed to the published version of the manuscript.

**Funding:** This work is supported by the National Science and Technology Council (Grant Nos. NTSC 111-2634-F-A49-007 and NTSC 111-2123-M-A49-001) and the Center for Emergent Functional Matter Science of National Yang Ming Chiao Tung University (NYCU) from The Featured Areas Research Center Program, within the framework of the Higher Education Sprout Project of the Taiwan Ministry of Education (MOE).

**Data Availability Statement:** Data can be obtained from the corresponding author upon a reasonable request.

**Conflicts of Interest:** The authors declare no conflict of interest.

## References

1. Protesescu, L.; Yakunin, S.; Bodnarchuk, M.I.; Krieg, F.; Caputo, R.; Hendon, C.H.; Yang, R.X.; Walsh, A.; Kovalenko, M.V. Nanocrystals of Cesium Lead Halide Perovskites (CsPbX<sub>3</sub>, X = Cl, Br, and I): Novel Optoelectronic Materials Showing Bright Emission with Wide Color Gamut. *Nano Lett.* **2015**, *15*, 3692–3696. [[CrossRef](#)]
2. Lin, K.; Xing, J.; Quan, L.N.; de Arquer, F.P.G.; Gong, X.; Lu, J.; Xie, L.; Zhao, W.; Zhang, D.; Yan, C.; et al. Perovskite Light-Emitting Diodes with External Quantum Efficiency Exceeding 20 per Cent. *Nature* **2018**, *562*, 245–248. [[CrossRef](#)]
3. Dey, A.; Ye, J.; De, A.; Debroye, E.; Ha, S.K.; Bladt, E.; Kshirsagar, A.S.; Wang, Z.; Yin, J.; Wang, Y.; et al. State of the Art and Prospects for Halide Perovskite Nanocrystals. *ACS Nano* **2021**, *15*, 10775–10981. [[CrossRef](#)]
4. Xing, G.; Mathews, N.; Lim, S.S.; Yantara, N.; Liu, X.; Sabba, D.; Grätzel, M.; Mhaisalkar, S.; Sum, T.C. Low-Temperature Solution-Processed Wavelength-Tunable Perovskites for Lasing. *Nat. Mater.* **2014**, *13*, 476–480. [[CrossRef](#)]
5. Geiregat, P.; Maes, J.; Chen, K.; Drijvers, E.; Roo, J.D.; Hodgkiss, J.M.; Hens, Z. Using Bulk-Like Nanocrystals to Probe Intrinsic Optical Gain Characteristics of Inorganic Lead Halide Perovskites. *ACS Nano* **2018**, *12*, 10178–10188. [[CrossRef](#)] [[PubMed](#)]
6. Yoo, J.J.; Seo, G.; Chua, M.R.; Park, T.G.; Lu, Y.; Rotermund, F.; Kim, Y.-K.; Moon, C.S.; Jeon, N.J.; Correa-Baena, J.-P.; et al. Efficient Perovskite Solar Cells via Improved Carrier Management. *Nature* **2021**, *590*, 587–593. [[CrossRef](#)] [[PubMed](#)]
7. Cui, J.; Liu, Y.; Deng, Y.; Lin, C.; Fang, Z.; Xiang, C.; Bai, P.; Du, K.; Zuo, X.; Wen, K.; et al. Efficient Light-Emitting Diodes Based on Oriented Perovskite Nanoplatelets. *Sci. Adv.* **2021**, *7*, eabg8458. [[CrossRef](#)] [[PubMed](#)]
8. Khan, J.; Zhang, X.; Yuan, J.; Wang, Y.; Shi, G.; Patterson, R.; Shi, J.; Ling, X.; Hu, L.; Wu, T.; et al. Tuning the Surface-Passivating Ligand Anchoring Position Enables Phase Robustness in CsPbI<sub>3</sub> Perovskite Quantum Dot Solar Cells. *ACS Energy Lett.* **2020**, *5*, 3322–3329. [[CrossRef](#)]
9. de Arquer, F.P.G.; Talapin, D.V.; Klimov, V.I.; Arakawa, Y.; Bayer, M.; Sargent, E.H. Semiconductor Quantum Dots: Technological Progress and Future Challenges. *Science* **2021**, *373*, eaaz8541. [[CrossRef](#)] [[PubMed](#)]
10. Ye, J.; Byrnavand, M.M.; Martínez, C.O.; Hoye, R.L.Z.; Saliba, M.; Polavarapu, L. Defect Passivation in Lead-Halide Perovskite Nanocrystals and Thin Films: Toward Efficient LEDs and Solar Cells. *Angew. Chem.* **2021**, *60*, 21636–21660. [[CrossRef](#)]
11. Ten Brinck, S.; Zaccaria, F.; Infante, I. Defects in Lead Halide Perovskite Nanocrystals: Analogies and (Many) Differences with the Bulk. *ACS Energy Lett.* **2019**, *4*, 2739–2747. [[CrossRef](#)]
12. du Fossé, I.; Mulder, J.T.; Almeida, G.; Spruit, A.G.M.; Infante, I.; Grozema, F.C.; Houtepen, A.J. Limits of Defect Tolerance in Perovskite Nanocrystals: Effect of Local Electrostatic Potential on Trap States. *J. Am. Chem. Soc.* **2022**, *144*, 11059–11063. [[CrossRef](#)] [[PubMed](#)]
13. Kong, L.; Zhang, X.; Zhang, C.; Wang, L.; Wang, S.; Cao, F.; Zhao, D.; Rogach, A.L.; Yang, X. Stability of Perovskite Light-Emitting Diodes: Existing Issues and Mitigation Strategies Related to Both Material and Device Aspects. *Adv. Mater.* **2022**, *34*, 2205217. [[CrossRef](#)]
14. Seth, S.; Ahmed, T.; De, A.; Samanta, A. Tackling the Defects, Stability, and Photoluminescence of CsPbX<sub>3</sub> Perovskite Nanocrystals. *ACS Energy Lett.* **2019**, *4*, 1610–1618. [[CrossRef](#)]
15. Wang, C.; Malinoski, A.; Yuan, J.; Brea, C.; Hu, G. A Surface Engineering Approach for Promoting Dexter Energy Transfer from Lead Halide Perovskite Nanocrystals. *J. Phys. Chem. C* **2023**, *127*, 1135–1144. [[CrossRef](#)]
16. Krieg, F.; Ochsenbein, S.T.; Yakunin, S.; Ten Brinck, S.; Aellen, P.; Süess, A.; Clerc, B.; Guggisberg, D.; Nazarenko, O.; Shynkarenko, Y.; et al. Colloidal CsPbX<sub>3</sub> (X = Cl, Br, I) Nanocrystals 2.0: Zwitterionic Capping Ligands for Improved Durability and Stability. *ACS Energy Lett.* **2018**, *3*, 641–646. [[CrossRef](#)]
17. Nenon, D.P.; Pressler, K.; Kang, J.; Koscher, B.A.; Olshansky, J.H.; Osowiecki, W.T.; Koc, M.A.; Wang, L.-W.; Alivisatos, A.P. Design Principles for Trap-Free CsPbX<sub>3</sub> Nanocrystals: Enumerating and Eliminating Surface Halide Vacancies with Softer Lewis Bases. *J. Am. Chem. Soc.* **2018**, *140*, 17760–17772. [[CrossRef](#)] [[PubMed](#)]
18. Koscher, B.A.; Swabeck, J.K.; Bronstein, N.D.; Alivisatos, A.P. Essentially Trap-Free CsPbBr<sub>3</sub> Colloidal Nanocrystals by Postsynthetic Thiocyanate Surface Treatment. *J. Am. Chem. Soc.* **2017**, *139*, 6566–6569. [[CrossRef](#)]
19. Fiuza-Maneiro, N.; Sun, K.; López-Fernández, I.; Gómez-Graña, S.; Müller-Buschbaum, P.; Polavarapu, L. Ligand Chemistry of Inorganic Lead Halide Perovskite Nanocrystals. *ACS Energy Lett.* **2023**, *8*, 1152–1191. [[CrossRef](#)]
20. Baek, S.-D.; Wang, C.; Khang, D.-Y.; Myoung, J.-M. Mixed Halide Perovskite Nanocrystals with Surface Engineering Based on Pseudohalide Passivation and Short-Chain Ligand Exchange for High-Performance Blue Light-Emitting Diodes. *Chem. Eng. J.* **2023**, *455*, 140594. [[CrossRef](#)]
21. Shen, X.; Kang, K.; Yu, Z.; Jeong, W.H.; Choi, H.; Park, S.H.; Stranks, S.D.; Snaith, H.J.; Friend, R.H.; Lee, B.R. Passivation Strategies for Mitigating Defect Challenges in Halide Perovskite Light-Emitting Diodes. *Joule* **2023**, *7*, 272–308. [[CrossRef](#)]
22. Yu, Y.; Tang, Y.; Wang, B.; Zhang, K.; Tang, J.; Li, Y. Red Perovskite Light-Emitting Diodes: Recent Advances and Perspectives. *Laser Photonics Rev.* **2023**, *17*, 2200608. [[CrossRef](#)]
23. DuBose, J.T.; Kamat, P.V. Surface Chemistry Matters. How Ligands Influence Excited State Interactions between CsPbBr<sub>3</sub> and Methyl Viologen. *J. Phys. Chem. C* **2020**, *124*, 12990–12998. [[CrossRef](#)]

24. Park, J.H.; Lee, A.-Y.; Yu, J.C.; Nam, Y.S.; Choi, Y.; Park, J.; Song, M.H. Surface Ligand Engineering for Efficient Perovskite Nanocrystal-Based Light-Emitting Diodes. *ACS Appl. Mater. Interfaces* **2019**, *11*, 8428–8435. [[CrossRef](#)] [[PubMed](#)]
25. Roo, J.D.; Ibáñez, M.; Geiregat, P.; Nedelcu, G.; Walravens, W.; Maes, J.; Martins, J.C.; Driessche, I.V.; Kovalenko, M.V.; Hens, Z. Highly Dynamic Ligand Binding and Light Absorption Coefficient of Cesium Lead Bromide Perovskite Nanocrystals. *ACS Nano* **2016**, *10*, 2071–2081. [[CrossRef](#)] [[PubMed](#)]
26. Pan, J.; Shang, Y.; Yin, J.; Bastiani, M.D.; Peng, W.; Dursun, I.; Sinatra, L.; El-Zohry, A.M.; Hedhili, M.N.; Emwas, A.-H.; et al. Bidentate Ligand-Passivated CsPbI<sub>3</sub> Perovskite Nanocrystals for Stable Near-Unity Photoluminescence Quantum Yield and Efficient Red Light-Emitting Diodes. *J. Am. Chem. Soc.* **2018**, *140*, 562–565. [[CrossRef](#)] [[PubMed](#)]
27. Yang, D.; Li, X.; Zhou, W.; Zhang, S.; Meng, C.; Wu, Y.; Wang, Y.; Zeng, H. CsPbBr<sub>3</sub> Quantum Dots 2.0: Benzenesulfonic Acid Equivalent Ligand Awakens Complete Purification. *Adv. Mater.* **2019**, *31*, e1900767. [[CrossRef](#)] [[PubMed](#)]
28. Dong, H.; Zhang, C.; Nie, W.; Duan, S.; Saggau, C.N.; Tang, M.; Zhu, M.; Zhao, Y.S.; Ma, L.; Schmidt, O.G. Interfacial Chemistry Triggers Ultrafast Radiative Recombination in Metal Halide Perovskites. *Angew. Chem. Int. Ed.* **2022**, *61*, e202115875. [[CrossRef](#)] [[PubMed](#)]
29. Imran, M.; Ijaz, P.; Goldoni, L.; Maggioni, D.; Petralanda, U.; Prato, M.; Almeida, G.; Infante, I.; Manna, L. Simultaneous Cationic and Anionic Ligand Exchange For Colloidally Stable CsPbBr<sub>3</sub> Nanocrystals. *ACS Energy Lett.* **2019**, *4*, 819–824. [[CrossRef](#)]
30. Malinoski, A.; Hu, G.; Wang, C. Strong Bidentate Coordination for Surface Passivation and Ligand-Shell Engineering of Lead Halide Perovskite Nanocrystals in the Strongly Quantum-Confinement Regime. *J. Phys. Chem. C* **2021**, *125*, 24521–24530. [[CrossRef](#)]
31. Zaccaria, F.; Zhang, B.; Goldoni, L.; Imran, M.; Zito, J.; van Beek, B.; Lauciello, S.; Trizio, L.D.; Manna, L.; Infante, I. The Reactivity of CsPbBr<sub>3</sub> Nanocrystals toward Acid/Base Ligands. *ACS Nano* **2022**, *16*, 1444–1455. [[CrossRef](#)] [[PubMed](#)]
32. Ravi, V.K.; Scheidt, R.A.; Nag, A.; Kuno, M.; Kamat, P.V. To Exchange or Not to Exchange. Suppressing Anion Exchange in Cesium Lead Halide Perovskites with PbSO<sub>4</sub>-Oleate Capping. *ACS Energy Lett.* **2018**, *3*, 1049–1055. [[CrossRef](#)]
33. Bhosale, S.S.; Narra, S.; Jokar, E.; Manikandan, A.; Chueh, Y.-L.; Diau, E.W.-G. Functionalized Hybrid Perovskite Nanocrystals with Organic Ligands Showing a Stable 3D/2D Core/Shell Structure for Display and Laser Applications. *J. Mater. Chem. C* **2021**, *9*, 17341–17348. [[CrossRef](#)]
34. Chang, C.-W.; Chou, C.K.; Chang, I.-J.; Lee, Y.-P.; Diau, E.W.-G. Relaxation Dynamics of Ruthenium Complexes in Solution, PMMA and TiO<sub>2</sub> Films: The Roles of Self-Quenching and Interfacial Electron Transfer. *J. Phys. Chem. C* **2007**, *111*, 13288–13296. [[CrossRef](#)]
35. Yamaguchi, S.; Hamaguchi, H.-O. Convenient Method of Measuring the Chirp Structure of Femtosecond White-Light Continuum Pulses. *Appl. Spectrosc.* **1995**, *49*, 1513–1515. [[CrossRef](#)]
36. Elliott, R.J. Intensity of Optical Absorption by Excitons. *Phys. Rev.* **1957**, *108*, 1384–1389. [[CrossRef](#)]
37. Awasthi, K.; Du, K.-B.; Wang, C.-Y.; Tsai, C.-L.; Hamada, M.; Narra, S.; Diau, E.W.-G.; Ohta, N. Electroabsorption Studies of Multicolored Lead Halide Perovskite Nanocrystalline Solid Films. *ACS Photonics* **2018**, *5*, 2408–2417. [[CrossRef](#)]
38. Narra, S.; Bhosale, S.S.; Kharade, A.K.; Chang, S.; Diau, E.W.-G. Retarded Charge Recombination to Enhance Photocatalytic Performance for Water-Free CO<sub>2</sub> Reduction Using Perovskite Nanocrystals as Photocatalysts. *J. Phys. Chem. Lett.* **2022**, *13*, 9134–9139. [[CrossRef](#)]
39. Tsai, I.-H.; Narra, S.; Bhosale, S.S.; Diau, E.W.-G. Energy and Charge Transfer Dynamics in Red-Emitting Hybrid Organo-Inorganic Mixed Halide Perovskite Nanocrystals. *J. Phys. Chem. Lett.* **2023**, *14*, 2580–2587. [[CrossRef](#)]
40. Giovanni, D.; Righetto, M.; Zhang, Q.; Lim, J.W.M.; Ramesh, S.; Sum, T.C. Origins of the Long-Range Exciton Diffusion in Perovskite Nanocrystal Films: Photon Recycling vs Exciton Hopping. *Light Sci. Appl.* **2021**, *10*, 2. [[CrossRef](#)]
41. Chirvony, V.S.; González-Carrero, S.; Suárez, I.; Galian, R.E.; Sessolo, M.; Bolink, H.J.; Martínez-Pastor, J.P.; Pérez-Prieto, J. Delayed Luminescence in Lead Halide Perovskite Nanocrystals. *J. Phys. Chem. C* **2017**, *121*, 13381–13390. [[CrossRef](#)]
42. Yamada, Y.; Nakamura, T.; Endo, M.; Wakamiya, A.; Kanemitsu, Y. Photocarrier Recombination Dynamics in Perovskite CH<sub>3</sub>NH<sub>3</sub>PbI<sub>3</sub> for Solar Cell Applications. *J. Am. Chem. Soc.* **2014**, *136*, 11610–11613. [[CrossRef](#)] [[PubMed](#)]
43. Price, M.B.; Butkus, J.; Jellicoe, T.C.; Sadhanala, A.; Briane, A.; Halpert, J.E.; Broch, K.; Hodgkiss, J.M.; Friend, R.H.; Deschler, F. Hot-Carrier Cooling and Photoinduced Refractive Index Changes in Organic-Inorganic Lead Halide Perovskites. *Nat. Commun.* **2015**, *6*, 8420. [[CrossRef](#)] [[PubMed](#)]
44. Fu, J.; Xu, Q.; Han, G.; Wu, B.; Huan, C.H.A.; Leek, M.L.; Sum, T.C. Hot Carrier Cooling Mechanisms in Halide Perovskites. *Nat. Commun.* **2017**, *8*, 1300. [[CrossRef](#)] [[PubMed](#)]
45. Rossi, D.; Wang, H.; Dong, Y.; Qiao, T.; Qian, X.; Son, D.H. Light-Induced Activation of Forbidden Exciton Transition in Strongly Confined Perovskite Quantum Dots. *ACS Nano* **2018**, *12*, 12436–12443. [[CrossRef](#)] [[PubMed](#)]
46. Knowles, K.E.; Malicki, M.; Weiss, E.A. Dual-Time Scale Photoinduced Electron Transfer from PbS Quantum Dots to a Molecular Acceptor. *J. Am. Chem. Soc.* **2012**, *134*, 12470–12473. [[CrossRef](#)]
47. Tao, S.; Schmidt, I.; Brocks, G.; Jiang, J.; Tranca, I.; Meerholz, K.; Olthof, S. Absolute Energy Level Positions in Tin- and Lead-Based Halide Perovskites. *Nat. Commun.* **2019**, *10*, 2560. [[CrossRef](#)]

**Disclaimer/Publisher's Note:** The statements, opinions and data contained in all publications are solely those of the individual author(s) and contributor(s) and not of MDPI and/or the editor(s). MDPI and/or the editor(s) disclaim responsibility for any injury to people or property resulting from any ideas, methods, instructions or products referred to in the content.